Lab on a Chip

PAPER

View Article Online
View Journal

Check for updates

Cite this: DOI: 10.1039/d6lc00301j

Droplet microfluidic profiling of NK cell cytotoxicity with machine learning-enabled target-cell death analysis

Rana S. Ozcan,[a] Fatemeh Vahedi,[bc] Shina Namakian,[bc] Ali A. Ashkar*[bc] and Tohid F. Didar *[ad]

Predicting the clinical efficacy of Natural Killer (NK) cell immunotherapies remains challenging due to functional heterogeneity within effector populations and tumor microenvironment (TME)-mediated suppression. Here, we present a droplet microfluidic platform that couples machine-learning-based, frame-wise K562 target-cell detection and live/dead classification with deterministic temporal event calling to map single-cell cytotoxicity trajectories at scale. These ML-derived target-cell trajectories were integrated with standardized morphology-based NK-cell annotation and effector-target attachment scoring. The resulting framework enabled standardized quantification of NK-cell cytotoxicity, serial-killing capacity, killing-time distributions, and attachment-linked outcomes across thousands of isolated NK-target microenvironments. Using matched donor-derived NK-cell states in defined single-effector droplets containing one to four K562 targets, we resolved how *ex vivo* expansion and ascites-mediated TME conditioning reshape individual NK-cell function. The results demonstrated that expanded NK cells (exNK) exhibited superior cytotoxic activity, serial killing, and rapid killing dynamics, whereas peripheral blood NK cells (pbNK), especially after exposure to ascites TME (pbNK-asc), showed reduced function across all cytotoxicity metrics. Notably, expanded NK cells exposed to ascites TME (exNK-asc) retained partial functionality, indicating that expansion provides resilience against suppressive factors. This single-cell platform provides insight into NK-cancer cell interactions and offers a scalable framework for optimizing off-the-shelf NK cell-based immunotherapies.

Received 11th April 2026,
Accepted 6th May 2026

DOI: 10.1039/d6lc00301j

rsc.li/loc

Open Access Article. Published on 13 May 2026. Downloaded on 6/3/2026 1:05:32 PM.
This article is licensed under a Creative Commons Attribution 3.0 Unported Licence.

1. Introduction

Natural Killer (NK) cells are critical components of the immune system, uniquely capable of detecting and eliminating cancer cells without prior sensitization.[1] Their ability to kill target cells directly and in an antigen-independent manner makes them promising agents for safe off-the-shelf cancer immunotherapies. Despite their potential, NK cell effectiveness varies significantly based on conditioning, phenotype, and exposure to the tumor microenvironment (TME), which can profoundly suppress their cytotoxic function.[2,3] Ascites fluid from ovarian cancer patients, rich in immunosuppressive factors, severely impairs NK cell activity,[4,5] while *ex vivo* expansion protocols enhance NK cell function.[6–8] Understanding how different NK cell states respond to immunosuppressive conditions is essential for optimizing NK cell-based immunotherapies, yet traditional bulk assays lack the resolution to capture functional heterogeneity and dynamic killing behavior at the single-cell level.[9,10]

Microfluidic devices have significantly advanced cellular research by enabling precise control of the cellular microenvironment,[11–14] facilitating high-throughput cytotoxicity assays, generation of stable chemical gradients,[15] single-cell analyses,[16] efficient cell sorting[17–19] and detection. Recent advances in droplet-based microfluidic platforms have enabled high-throughput and per-cell analysis of NK cell-mediated cytotoxicity.[20–23] These platforms allow evaluation of NK cell killing efficiency, cytokine secretion, and functional heterogeneity at the individual cell level. Others have integrated these platforms with transcriptomic, genotypic, and secretomic profiling to assess CAR-NK cell responses and therapeutic efficacy.[24,25] Additionally, microfluidic systems have been employed to model the TME and evaluate drug responses in complex settings[26–28] offering powerful tools for

[a] *School of Biomedical Engineering, McMaster University, Hamilton, Ontario, Canada L8S 4L7. E-mail: didar@mcmaster.ca*
[b] *McMaster Immunology Research Center, Department of Medicine, McMaster University, Hamilton, Ontario, Canada L8N 3Z5. E-mail: ashkara@mcmaster.ca*
[c] *Centre for Discovery in Cancer Research, McMaster University, Hamilton, Ontario, Canada L8S 4M1*
[d] *Department of Mechanical Engineering, McMaster University, Hamilton, Ontario, Canada L8S 4L7*

Open Access Article. Published on 13 May 2026. Downloaded on 6/3/2026 1:05:32 PM.
This article is licensed under a Creative Commons Attribution 3.0 Unported Licence.

both basic immunology and translational cancer research. Finally, droplet-recovery methods now enable retrieval of live NK and target cells after screening, linking function to downstream profiling.[29] The integration of machine learning approaches into these platforms has further advanced automated analysis capabilities for droplet and cell identification.[30,31]

Although prior droplet-based NK-cell studies have established single-cell functional heterogeneity, serial killing, and in some cases automated fluorescence-based droplet analysis or combined cytotoxicity-and-secretion profiling, these studies addressed different biological comparisons and analytical emphases than the present work. Prior reports have examined NK-92 cells,[20,26] other NK products,[23] and donor-level heterogeneity,[22] but, to our knowledge, have not systematically compared matched-donor freshly isolated peripheral-blood NK cells and feeder-expanded peripheral-blood NK cells together with their corresponding malignant-ascites-conditioned states within a single droplet-based framework. In parallel, there remains a need for analytical workflows that convert full 10-hour image sequences into standardized per-droplet cytotoxicity trajectories using transparent and reproducible event-calling rules rather than relying primarily on endpoint summaries or less explicitly defined temporal outputs. Therefore, the contribution of this study is not the first demonstration of droplet-based single-cell NK profiling itself, but the integration of a matched-donor, four-state biological comparison with a machine-learning-enabled, frame-wise target-detection pipeline and deterministic temporal event-calling workflow for standardized extraction of killing frequency, serial killing, killing kinetics, and attachment-linked outcomes across large droplet datasets. This integrated approach is important for identifying functionally distinct NK-cell products and for understanding how *ex vivo* expansion may alter susceptibility to TME-like suppression as NK-cell therapies continue to advance toward clinical application.[32,33]

Here, we present a droplet-based microfluidic platform for time-resolved, single-cell profiling of four clinically relevant NK-cell states: freshly isolated peripheral-blood NK cells (pbNK), malignant-ascites-conditioned pbNK (pbNK-asc), *ex vivo* expanded NK cells (exNK), and malignant-ascites-conditioned exNK (exNK-asc). By generating all four conditions from matched donors, this design minimizes inter-donor variability and enables functional differences to be attributed more directly to expansion and TME-like conditioning. Within defined nanoliter droplets containing one NK cell and one to four K562 targets, NK-target interactions were monitored over 10 hours by time-lapse microscopy. The analysis workflow combines machine-learning-enabled, frame-wise K562 target-cell detection and live/dead classification with standardized manual annotation of NK enumeration, NK viability, and NK-target attachment outcomes in droplets. These outputs are integrated through deterministic temporal event-calling to generate per-droplet cytotoxicity trajectories and quantify cytotoxic NK-cell frequency, serial killing capacity, killing kinetics, and attachment-linked outcomes. This framework enables matched, single-effector functional benchmarking of NK-cell products and reveals how *ex vivo* expansion modulates resilience to ascites-mediated TME suppression.

2. Results

2.1. Droplet microfluidic assay overview

Natural killer cells represent a cornerstone of innate immunity, eliminating transformed cells through direct cytotoxic mechanisms without requiring prior antigen exposure. This effector function relies on formation of an immunological synapse at the NK-target interface, followed by polarized secretion of lytic granules containing perforin and granzymes that trigger apoptotic cascades in cancer cells (Fig. 1a). While this contact-dependent killing pathway forms the mechanistic basis for NK cell immunotherapy,[34] conventional population-level cytotoxicity assays obscure critical functional parameters. Bulk measurements cannot identify the fraction of cytotoxic effectors within heterogeneous NK populations, quantify serial killing capacity, or resolve kinetic differences in target elimination rates (Fig. S1). These single-cell behaviors directly determine therapeutic efficacy, particularly in solid tumors where effector-to-target ratios are unfavorable and only a subset of infused NK cells may retain cytotoxic competence.

To overcome these analytical limitations, we used a droplet-based microfluidic system that partitions NK and target cells into nanoliter-scale aqueous compartments, enabling longitudinal tracking of cytotoxic events at single-cell resolution (Fig. 1b and Movie S1). The platform centers on a commercial droplet generation and storage chip (Fluidic 719, ChipShop) that integrates a flow-focusing junction with an on-chip trapping array. NK cells were loaded at 2×10^5 cells per mL and K562 at 1×10^6 cells per mL, with measured droplet diameter of 176.4 ± 3.9 μm suspended in fluorinated carrier oil containing 2% biocompatible surfactant (dSurf). Captured droplets remain anchored in microfluidic trap structures throughout the experiment, maintaining stable 37 °C temperature and 5% CO_2 atmosphere during 10-hour time-lapse acquisition at 15-minute intervals (Fig. 1b and S2).

Representative brightfield microscopy shows the NK, K562, and dSurf streams at the flow-focusing junction during droplet generation (Fig. 1c). This configuration produces droplets containing variable combinations of effectors and targets that can be monitored over time under controlled imaging conditions.

A critical technical advantage of our approach stems from the use of genetically engineered K562 cells stably expressing the mKate2 far-red fluorescent protein, enabling longitudinal imaging without exogenous viability dyes. The fluorescent signal remains stable throughout the 10-hour observation window, and changes in fluorescence intensity and spatial distribution support target cell viability assessment.

 This journal is © The Royal Society of Chemistry 2026

Open Access Article. Published on 13 May 2026. Downloaded on 6/3/2026 1:05:32 PM.
This article is licensed under a Creative Commons Attribution 3.0 Unported Licence.

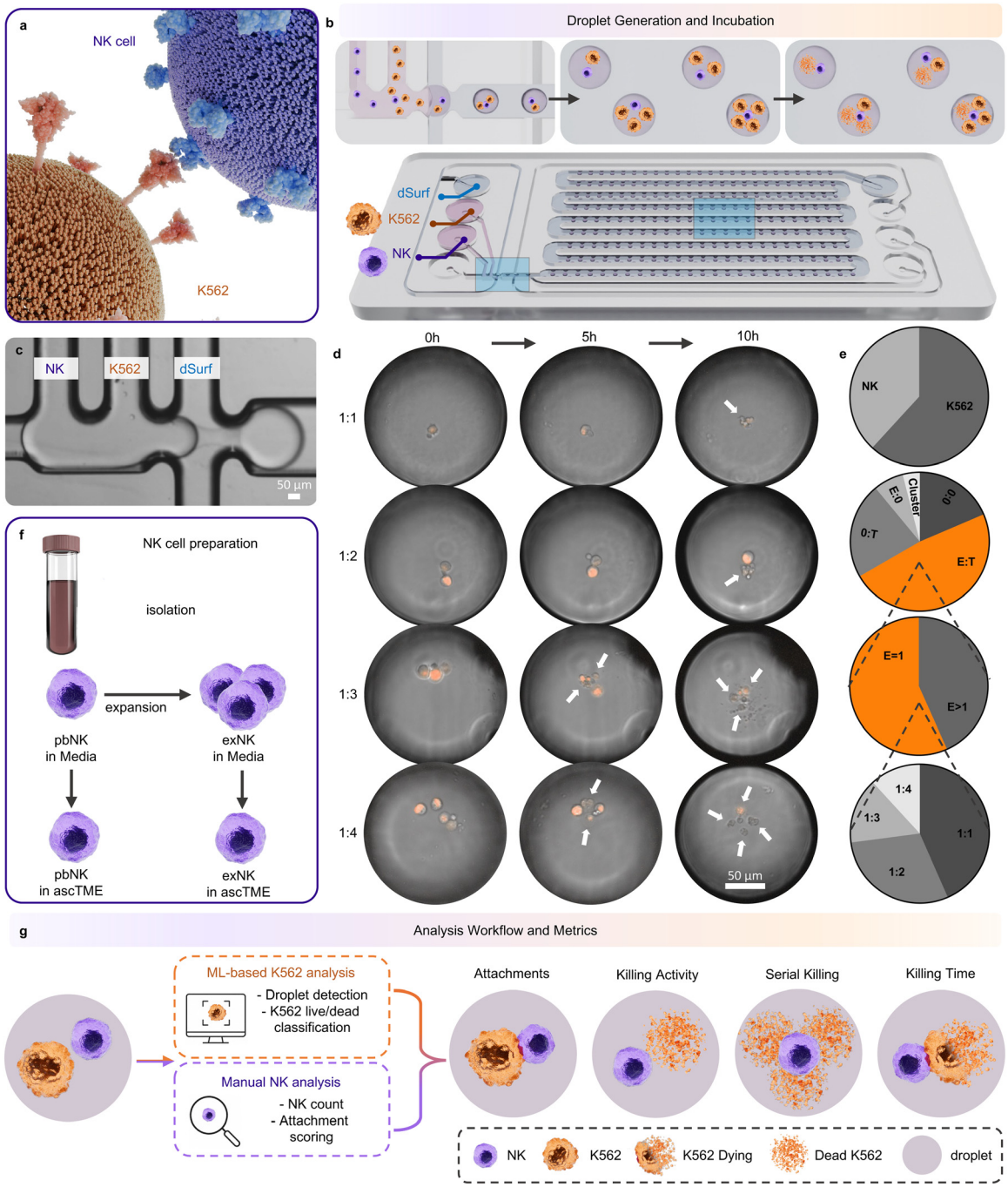

Fig. 1 Single-cell analysis of NK cell cytotoxicity in a droplet microfluidic platform. (a) Illustration depicting NK cell-mediated cytotoxicity against K562 tumor cells. NK cell recognizes and attacks K562 tumor cell through directed cytotoxic mechanisms. (b) Droplet generation and incubation. Top: schematic of the flow-focusing process where NK cells (purple) and K562 target cells (orange) are co-encapsulated with dSurf oil to form droplets. Bottom: microfluidic chip (Fluidic 719) showing droplet array storage for 10-hour time-lapse imaging. (c) Representative brightfield microscopy image of the flow-focusing junction showing the NK, K562, and dSurf inlet streams during droplet generation. Scale bar, 50 μm. (d) Representative time-lapse images showing NK cell interactions with K562 cells over 10 hours at varying effector-to-target (E : T) ratios (1 : 1, 1 : 2, 1 : 3, 1 : 4) using 10× magnification. K562 cells appear as orange fluorescent spots (TRITC overlay). White arrows highlight dead K562 cells. Scale bar, 50 μm. (e) Quantification of droplet contents. Top to bottom: distribution of detected cell types across droplets (NK and K562); distribution of droplet classes including empty droplets (0 : 0), co-encapsulated droplets (E : T), K562-only droplets (0 : T), NK-only droplets (E : 0), and droplets with cell clusters; distribution of E : T droplets by NK cell number (E = 1 for single NK cell, $E > 1$ for multiple NK cells); and distribution of E = 1 droplets by K562 number from 1 to 4. (f) Schematic illustrating NK cell preparation workflow: isolation from peripheral blood, *ex vivo* expansion, and conditioning in ascites tumor microenvironment (ascTME) to generate four NK cell states: pbNK, exNK, pbNK-asc, and exNK-asc. (g) Analysis workflow and output metrics derived from droplet time-lapse imaging. K562-related analysis was performed using an ML-based workflow for droplet detection and K562 live/dead classification, whereas NK-related outputs were obtained from morphology-guided NK counting and attachment scoring in the time-lapse images. These complementary analyses were integrated to quantify attachment outcomes, killing activity, serial killing, and killing time.

Open Access Article. Published on 13 May 2026. Downloaded on 6/3/2026 1:05:32 PM. This article is licensed under a Creative Commons Attribution 3.0 Unported Licence.

Representative time-lapse images show NK cell interactions with K562 cells across droplets containing different effector-to-target (E : T) ratios from 1 : 1 to 1 : 4 (Fig. 1d). Intact viable target cells exhibit compact morphology and retained fluorescence, whereas dying cells display characteristic blebbing, fragmentation, and altered fluorescent signal distribution.

Quantitative analysis of droplet composition revealed robust encapsulation efficiency and a distribution of droplet classes suitable for single-cell functional profiling (Fig. 1e). Approximately 48% of droplets in imaged regions contained co-encapsulated NK-K562 pairs, with the remaining fraction split between empty droplets, single-cell-type compartments, and rare multi-cell aggregates. Among productive co-culture droplets, 56.7% comprised single-NK configurations (E = 1) paired with one to four K562 targets, representing the optimal geometry for resolving individual effector behavior. This distribution spans physiologically relevant E : T ratios from 1 : 1, permitting assessment of maximal per-cell cytotoxicity, to 1 : 4, challenging NK cells with target-rich conditions that test serial killing capacity.

We next established four clinically relevant NK cell phenotypes to examine how *ex vivo* expansion and tumor-microenvironment conditioning influence cytotoxic function (Fig. 1f). Peripheral blood NK cells (pbNK) freshly isolated from healthy donors *via* magnetic negative selection served as the baseline effector population. *Ex vivo* expanded NK cells (exNK) were generated through three-week co-culture with irradiated K562-mbIL21 feeder cells in the presence of exogenous IL-2, following established protocols that enhance proliferative capacity and cytotoxic potency.[35] To model immunosuppressive tumor microenvironment exposure, both pbNK and exNK populations were conditioned in cell-free malignant ascites fluid collected from ovarian cancer patients for three days, yielding pbNK-asc and exNK-asc cohorts. Malignant ascites contains soluble immunosuppressive mediators, including TGF-β, IL-10, and IL-6, that suppress NK cell receptor signaling, cytokine production, and degranulation responses,[35,36] thereby recapitulating key features of the hostile environment that limits NK cell efficacy in solid tumors (Fig. S3). Importantly, all four NK states were derived from identical donor samples, minimizing inter-donor variability and enabling direct attribution of functional differences to conditioning regimens. After establishing these matched NK-cell states, we confirmed that isolated NK cells from each condition, as well as K562 targets, remained largely viable over the 10-hour droplet-imaging window, with minimal spontaneous death under the assay conditions (Fig. S4).

Using this platform, we resolved four complementary functional parameters from droplet time-lapse imaging (Fig. 1g). Attachment frequency and duration quantify physical NK-target contact, the prerequisite for immunological synapse formation and granule polarization. Killing activity identifies the fraction of NK cells capable of eliminating at least one target, distinguishing cytotoxic from non-cytotoxic effectors within heterogeneous populations. Serial killing captures the ability of individual NK cells to sequentially engage and destroy multiple targets, a critical determinant of therapeutic efficacy when effector-to-target ratios are unfavorable. Killing time measures the interval from initial attachment to target cell death, providing a direct readout of the kinetics of NK-cell-mediated cytotoxicity. Together, these measurements provide a comprehensive framework for comparing the functional behavior of clinically relevant NK cell states at single-cell resolution.

2.2. Machine learning-enabled target-cell detection and temporal death-event calling

High-throughput functional profiling of NK-cell cytotoxicity requires an analysis workflow that can process large numbers of droplets while preserving single-cell and time-resolved information.[37] In the context of NK-cell immunotherapy, automating the identification of target-cell death across extended time-lapse sequences is essential for capturing rare behaviors such as serial killing and for resolving kinetic heterogeneity that bulk assays obscure.[38,39] Manual annotation of target-cell death across such datasets is labor-intensive and susceptible to observer bias, particularly when distinguishing subtle morphological changes associated with target-cell death. We therefore developed a semi-automated analysis pipeline in which the machine-learning component was used for droplet detection and K562 target-cell live/dead classification, while NK-related annotations were performed manually using standardized morphology-based criteria to extract droplet-level cytotoxicity trajectories at scale.

The automated component of the workflow is summarized in Fig. 2a. To identify K562 target cells and classify their viability state, we used YOLO (You Only Look Once), a single-pass object-detection architecture that localizes and classifies multiple objects in one forward pass. The model was trained on annotated brightfield-TRITC overlay images using Roboflow (Roboflow 3.0 Object Detection [Accurate]). The training dataset comprised 198 images (2048 × 2044 pixels) spanning diverse droplet configurations, cell densities, and viability states, with 3675 total annotations across three classes: droplets (1343), viable K562 cells (1764), and dead K562 cells (568). Source images were split 92/4/4% into training, validation, and test partitions before augmentation. High-resolution images were tiled for all three splits, and additional augmentations, including horizontal and vertical flips, rotation, brightness adjustment, and blur perturbations, were applied only to the training set, yielding 4266 training images, 180 validation images, and 180 test images. Training was conducted for 50 epochs with best-checkpoint selection at checkpoint 4. Validation performance reached 90.9% mAP@50, with per-class AP values of 97% for droplets, 97% for viable K562 cells, and 79% for dead K562 cells. On the held-out test set, the model achieved 85.8% precision and 91.3% recall.

This journal is © The Royal Society of Chemistry 2026

Open Access Article. Published on 13 May 2026. Downloaded on 6/3/2026 1:05:32 PM.
This article is licensed under a Creative Commons Attribution 3.0 Unported Licence.

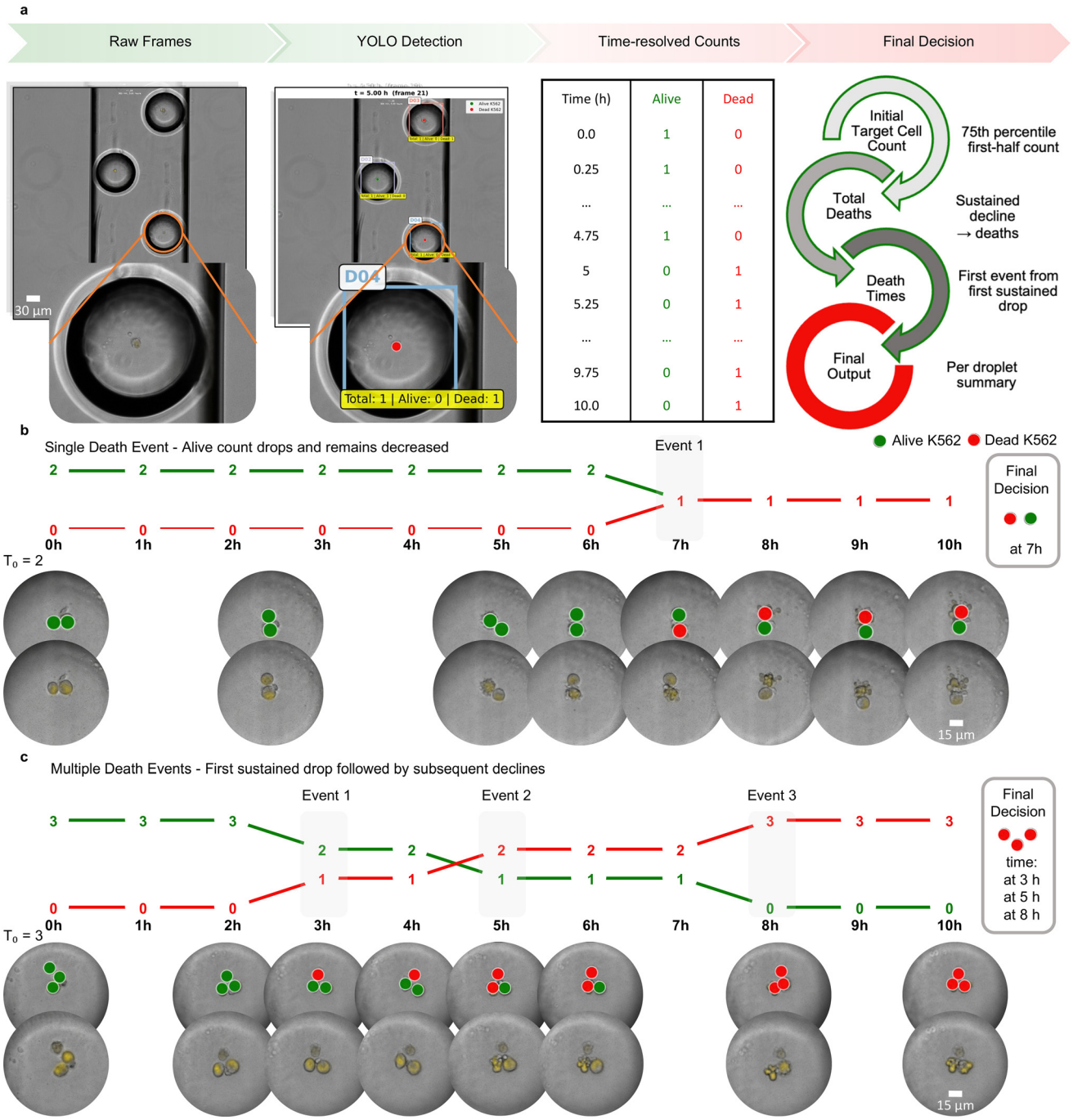

Fig. 2 Automated pipeline for time-resolved identification of NK cell-mediated target cell death in droplet microfluidics. (a) Representative workflow illustrating the analysis pipeline. Raw brightfield-TRITC image frames are processed using a YOLO-based detector to identify droplets and classify K562 target cells as alive or dead at each time point across the full 10 h sequence. Frame-wise per-droplet counts of alive (green) and dead (red) K562 cells are used to generate time-resolved trajectories. These trajectories are then converted into droplet-level outputs by estimating the initial target count using the 75th percentile of first-half counts, determining the total number of deaths from sustained declines in alive-target signal, and assigning death times from the corresponding decline events. Final outputs are reported on a per-droplet basis as initial target count, total deaths, and death times. (b) Example of a single death event within an individual droplet with an initial target count of T_0 = 2. The number of alive target cells remains constant until a single transition from 2 to 1 is observed, and this decrease persists over subsequent frames. The droplet is therefore assigned one death event at 7 h. (c) Example of multiple death events within an individual droplet with an initial target count of T_0 = 3. Sequential sustained decreases in alive-target counts are observed over time, corresponding to three accepted death events. These events are assigned to 3 h, 5 h, and 8 h, yielding a final output of three deaths in the droplet.

At inference, the detector was applied to all 41 frames acquired over the 10 h imaging window at 15 min intervals, thereby generating full-sequence frame-wise outputs rather than endpoint-only measurements (Fig. 2a and Movie S2).

Open Access Article. Published on 13 May 2026. Downloaded on 6/3/2026 1:05:32 PM.
This article is licensed under a Creative Commons Attribution 3.0 Unported Licence.

Class-specific confidence thresholds were intentionally set below the training optimum to favor recall at the frame level, namely 20% for droplets, 2.5% for viable K562 cells, and 3.0% for dead K562 cells, with a 25% IoU threshold for non-maximum suppression. Droplets were identified first, and K562 cells were assigned to droplets by geometric containment of the cell center within the droplet boundary. Droplets were then linked across frames by nearest-neighbor spatial matching using a 75 px Euclidean distance threshold, preserving consistent droplet identities throughout the sequence. For each droplet and each frame, the pipeline exported total, alive, and dead K562 counts, which formed the input for downstream temporal analysis.

To convert these frame-wise detections into robust droplet-level outputs, we decoupled target-count estimation, death counting, and death timing. The initial number of target cells per droplet was estimated from the 75th percentile of nonzero total-cell detections in the first half of the experiment, a strategy designed to compensate for under-detection in crowded droplets while avoiding distortion from later death-associated count loss. Droplets with estimated target counts greater than four were classified as clusters and excluded from downstream cytotoxicity calculations. The total number of deaths per droplet was then inferred from sustained declines in the smoothed alive-target trajectory over the course of the experiment, with dead-cell corroboration used to reduce over-calling in multi-cell droplets. Finally, death times were assigned from the trajectory itself by identifying the first sustained decline event and, where applicable, additional later decline events, thereby converting frame-wise detections into standardized per-droplet time-resolved killing outputs (Fig. 2a). This count-and-timing framework was designed to reduce sensitivity to frame-level detection noise while preserving the temporal structure of individual killing trajectories.

Fig. 2b shows a representative example of a single death event in a droplet with an initial target count of $T_0 = 2$. In this droplet, the alive-target count remains stable through the early portion of the sequence and then decreases from 2 to 1 at 7 h, after which it remains decreased. The droplet is therefore assigned one death event at 7 h. Although only representative hourly frames are displayed for clarity, the decision is made from the full 41-frame trajectory. Fig. 2c shows a representative example of multiple death events in a droplet with an initial target count of $T_0 = 3$. In this case, the first sustained decline in alive-target count is followed by additional later declines, corresponding to three accepted death events. These events are assigned to 3 h, 5 h, and 8 h, respectively. This analysis framework therefore captures not only whether killing occurred, but also how many sequential killing events were performed within an individual droplet and when those events occurred.

Because NK cells were not identified by the YOLO detector, NK enumeration, viability scoring, and attachment annotation were performed manually using standardized morphology-based criteria. Within droplets, single-cell viability controls showed minimal spontaneous death of isolated NK cells over the 10 h imaging window (Fig. S4), supporting the compatibility of the droplet environment with NK-cell survival during the assay. To validate NK cell annotations, we compared brightfield morphology calls against an orthogonal live/dead assay using FVS520 staining (Fig. S5). Representative matched brightfield and fluorescence images, concordant and mismatch examples, and confusion-matrix-based performance metrics showed good agreement between brightfield-based scoring and FVS520 status. These results support the use of morphology-based NK viability assessment within the hybrid analysis framework; however, because the FVS520 validation was performed outside droplets, it should be interpreted as validation of the brightfield morphological criteria rather than direct validation under all droplet-confined interaction states. Nevertheless, because NK cells can deform during prolonged target engagement, manual viability scoring may occasionally misclassify transiently deformed but viable NK cells or conversely fail to identify early non-viable cells before overt fragmentation. We therefore interpret NK-side metrics as morphology-based estimates, with the potential effects of viability misclassification considered in the Discussion.

We next benchmarked the machine learning-enabled workflow against blinded expert reference annotations across all four functional outputs (Fig. S6). The automated analysis showed strong agreement with manual scoring for percentage target killing, percentage cytotoxic NK cells, percentage serial killer NK cells, and average killing time across pbNK, pbNK-asc, exNK, and exNK-asc conditions. Correlation coefficients exceeded 0.85 for target-cell killing and cytotoxic NK-cell identification, and agreement remained robust for serial killer frequencies and killing-time measurements. Paired comparisons showed no significant differences across the assessed conditions. These results indicate that the semi-automated pipeline captures biologically meaningful differences between NK-cell states with fidelity comparable to expert curation.

Overall, this integrated semi-automated workflow addresses a central limitation of droplet-based NK assays by converting full 10 h, frame-wise image sequences into standardized per-droplet cytotoxicity trajectories at scale. The combination of automated K562 detection, robust target-count estimation, decline-based death calling, and validated morphology-based NK scoring enables reproducible quantification of killing fraction, cytotoxic NK-cell frequency, serial killing, and killing kinetics across large droplet datasets, thereby providing the analytical framework needed for rigorous comparison of clinically relevant NK-cell states.

2.3. Attachment dynamics reflect functional diversity of NK cells

Physical contact between NK cells and target cells is a prerequisite for effective cytotoxicity, as it enables formation of the immunological synapse, a specialized membrane

 This journal is © The Royal Society of Chemistry 2026

Open Access Article. Published on 13 May 2026. Downloaded on 6/3/2026 1:05:32 PM.
This article is licensed under a Creative Commons Attribution 3.0 Unported Licence.

interface through which lytic granules containing perforin and granzymes are directionally released to induce target cell death.[34] Defects in NK cell attachment or synapse stabilization compromise therapeutic efficacy in cancer immunotherapy, particularly in solid tumors where physical barriers and immunosuppressive factors impede effector-target interactions.[40] Understanding how conditioning regimens and TME exposure influence NK cell attachment behavior is therefore critical for optimizing cell-based therapies.

To systematically quantify attachment dynamics, we developed a scoring method based on time-lapse microscopy. NK cells and K562 targets were visually assessed at 15-minute intervals over 10 hours, with membrane contact persisting across three or more consecutive frames (≥30 minutes) scored as an attachment event. This temporal threshold distinguished transient collisions from stable interactions capable of supporting synapse formation. Scoring was performed by blinded observers using standardized criteria to ensure reproducibility: physical contact was defined as visible overlap or adjacency of cell boundaries, confirmed across sequential frames to eliminate ambiguous calls. During attachment scoring, the same NK cell was manually followed within each single-NK droplet across adjacent frames using its lack of TRITC signal, smaller size relative to K562 cells, morphology, and positional continuity, allowing tracking even when transient deformation occurred during target engagement. Killing outcomes were independently determined by the automated YOLO-based detection pipeline described above, enabling unbiased correlation of attachment behavior with cytotoxic function.

NK-target interactions resolved into three discrete outcomes at the target-cell level within single-NK droplets: no attachment (the NK cell does not contact a given target), attachment without killing (contact is established but the target survives), and attachment with killing (contact culminates in target lysis) (Fig. 3a). These categories capture sequential decision points in the cytotoxic cascade, including target encounter, stable contact, and progression from contact to lysis, each of which can be modulated by NK-cell functional state. Representative microscopy images illustrate the spectrum of behaviors across conditions (Fig. 3b). Peripheral-blood NK cells, particularly pbNK-asc, more frequently exhibited non-productive outcomes, whereas expanded NK cells displayed more frequent attachment with killing.

Quantification of interaction outcomes revealed striking differences among NK-cell phenotypes (Fig. 3c). pbNK-asc cells demonstrated the highest frequency of no attachment (around 20%) and the lowest attachment-and-killing fraction (6%), consistent with functional impairment induced by ascites-derived immunosuppressive factors. In contrast, exNK cells showed the lowest no-attachment rate (2%) and the highest attachment-and-killing frequency, reaching 46%, reflecting enhanced target engagement and effector capacity conferred by *ex vivo* expansion. Intermediate phenotypes emerged for pbNK and exNK-asc populations, with pbNK showing attachment-and-killing in 21% of interactions and exNK-asc retaining partial cytotoxic function, with productive interactions in 27% of cases despite TME conditioning. Together, these findings indicate that expansion promotes productive progression from contact to lysis, whereas ascites exposure shifts interactions toward non-productive outcomes.

When interaction outcomes were pooled across NK phenotypes, the overall distribution remained broadly similar across E : T ratios (Fig. 3d). No-attachment events stayed low across all ratios, ranging from 6% to 12%. Only-attachment outcomes accounted for the majority of interactions, remaining between 72% and 79% across all ratios, whereas attachment-and-killing events were lower at 1 : 1 and 1 : 2 (20%) and modestly higher at 1 : 3 and 1 : 4, reaching 27% and 30%, respectively. Only modest shifts were observed with increasing target density, consistent with changes in encounter opportunities rather than a major change in execution efficiency. These data suggest that intrinsic NK-cell functional state contributes more strongly than target availability to whether contact progresses to productive killing.

To further resolve attachment behavior during sequential killing and to visually confirm NK tracking during engaged states, we examined representative time-lapse sequences from single-NK droplets (Fig. 3e). In these droplets, the same effector was followed frame to frame based on its persistent TRITC-negative signal, smaller size relative to K562 cells, and positional continuity across the sequence, even when transiently deformed during target engagement. Two distinct patterns were observed. In Pathway I, the NK cell contacted T1, induced T1 lysis, detached, and later reengaged T2. In Pathway II, the NK cell maintained continuous or near-continuous contact through sequential interactions, with T2 engagement occurring without a clearly separated detached interval after T1 lysis. Thus, sequential killing did not require one obligate attachment pattern. A second lytic event could occur either after a detached interval or during sustained contact. Although these image sequences do not directly measure granule reloading, they show that detachment from the first killed target is not strictly required before engagement of a subsequent target.

These results establish attachment dynamics as a distinct and informative layer of NK-cell functional heterogeneity. The platform resolves not only whether a target is killed, but also whether failure occurs at the level of target encounter, sustained attachment, or progression from contact to lysis. By combining time-resolved attachment scoring with automated target-death calling, this workflow distinguishes productive from non-productive engagement states and shows that sequential attachments can proceed through more than one contact pattern.

2.4. Cytotoxicity and serial killing reveal functional hierarchies among NK cell states

Serial killing capacity, the ability of a single NK cell to sequentially eliminate multiple targets, is a critical

Open Access Article. Published on 13 May 2026. Downloaded on 6/3/2026 1:05:32 PM.
This article is licensed under a Creative Commons Attribution 3.0 Unported Licence.

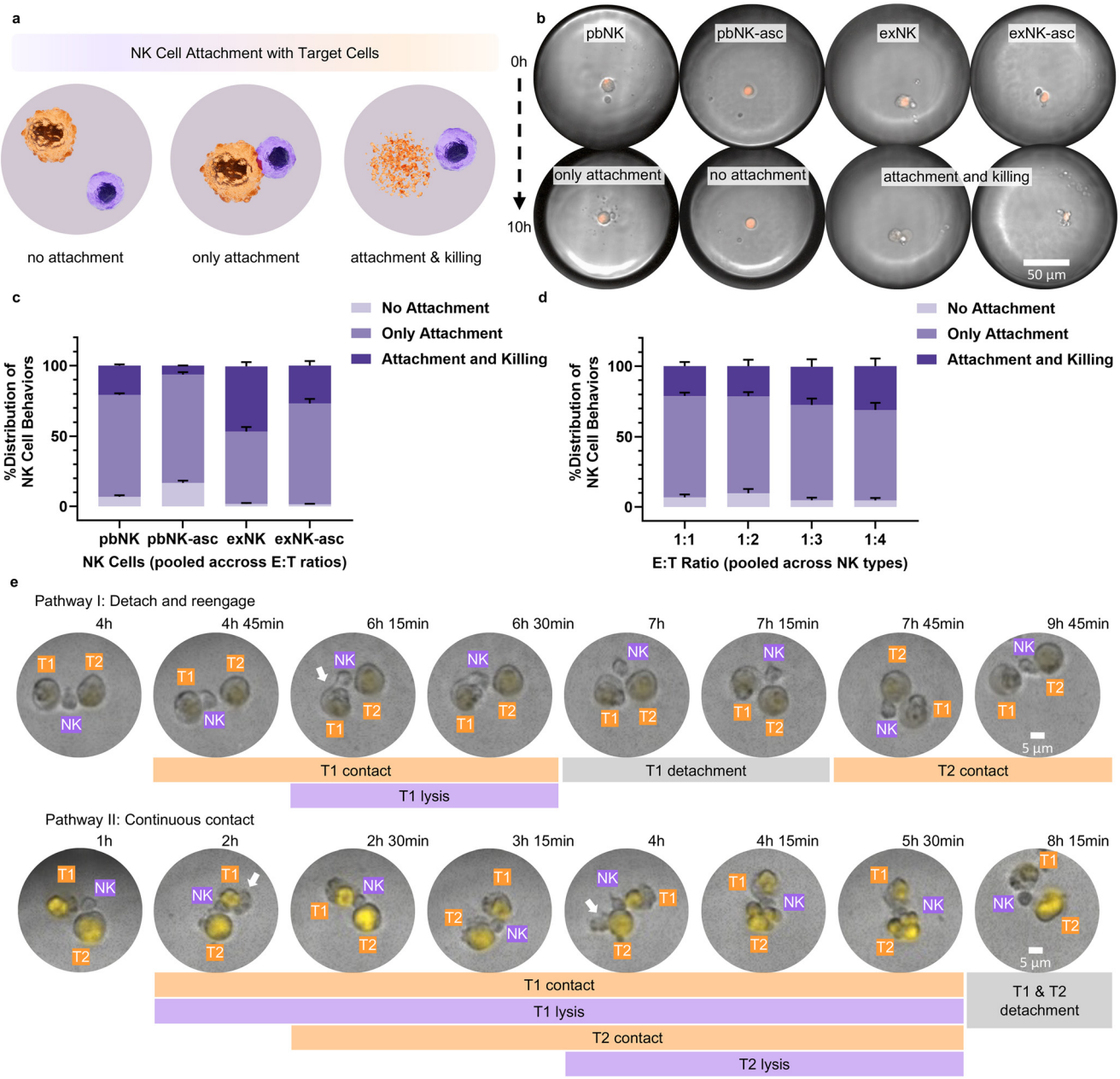

Fig. 3 NK cell attachment dynamics and interaction outcomes with K562 target cells. (a) Schematic illustrating three categories of NK cell behavior toward K562 targets: no attachment (NK cell does not contact target), only attachment (NK cell contacts target but does not kill), and attachment and killing (NK cell contacts target and induces target death). Purple cells represent NK cells; orange represents K562 target cells. (b) Representative microscopic images showing NK cell attachment outcomes across different NK cell states. Top row: initial droplet configurations for pbNK, pbNK-asc, exNK, and exNK-asc conditions at early time points. Bottom row: representative examples of the three interaction outcomes at 10 h, including only attachment, no attachment, and attachment and killing. Images were acquired at 10× magnification. Scale bar, 50 μm. (c) Distribution of NK cell interaction outcomes by NK cell type. Stacked bars show the percentage of K562 target-cell interaction outcomes classified as no attachment, only attachment, or attachment and killing for each condition. Data were pooled across the tested E : T ratios within each NK phenotype: pbNK (n = 390), pbNK-asc (n = 392), exNK (n = 451), and exNK-asc (n = 365). n denotes the total number of K562 target cells analyzed across three biological replicates. (d) Distribution of NK cell interaction outcomes across varying effector-to-target (E : T) ratios. For each E : T ratio, interaction outcomes were pooled across NK phenotypes (pbNK, pbNK-asc, exNK, exNK-asc) within each biological replicate: 1 : 1 (n = 275), 1 : 2 (n = 480), 1 : 3 (n = 531), and 1 : 4 (n = 312). n denotes the total number of K562 target cells analyzed across three biological replicates. Error bars represent SEM. (e) Representative time-lapse sequences illustrating two interaction patterns observed in single-NK droplets. Pathway I: detach and reengage. The NK cell first establishes contact with target cell 1 (T1), with T1 lysis indicated by a white arrow at the corresponding stage, before detaching and subsequently reattaching to target cell 2 (T2). Pathway II: continuous contact. The NK cell first contacts T1, induces T1 lysis, then engages T2 without a clearly separated detached interval, followed by T2 lysis before eventual disengagement. NK cells are labeled in purple and K562 target cells are labeled in orange. White arrows indicate target-cell lysis. Bars beneath each sequence summarize the timing of contact, lysis, and detachment events. Scale bars, 5 μm.

This journal is © The Royal Society of Chemistry 2026

Open Access Article. Published on 13 May 2026. Downloaded on 6/3/2026 1:05:32 PM.
This article is licensed under a Creative Commons Attribution 3.0 Unported Licence.

determinant of therapeutic efficacy in cancer immunotherapy.[41] In the tumor microenvironment, effector-to-target ratios are often highly unfavorable, with cancer cells vastly outnumbering infiltrating immune cells.[42] Under these conditions, NK cells capable of serial killing can exert disproportionate anti-tumor effects, compensating for numerical disadvantages through repeated target engagement.[43] Traditional bulk cytotoxicity assays, which measure population-level killing without resolving individual effector behavior, cannot distinguish serial killers from single-hit effectors or identify non-cytotoxic cells within heterogeneous populations. Quantifying these functionally distinct subsets is essential for predicting therapeutic outcomes and selecting optimal NK cell products for clinical translation.

We stratified NK cells into three functional categories based on target elimination capacity: non-cytotoxic NK cells (fail to kill any targets), cytotoxic NK cells (eliminate at least one target), and serial killer NK cells (sequentially eliminate multiple targets) (Fig. 4a). This classification captures the full spectrum of NK cell functionality, from inactive effectors that may represent exhausted or inhibited states to highly active serial killers that drive sustained anti-tumor responses. Representative time-lapse microscopy images illustrate the marked differences in killing behavior across NK cell phenotypes at 0 and 10 hours (Fig. 4b). Droplets containing pbNK-asc cells consistently showed minimal target elimination, with K562 cells remaining intact throughout the observation period. In contrast, exNK droplets exhibited pronounced cytotoxic activity, with visible evidence of target fragmentation.

Target cell killing efficiency, quantified as the percentage of K562 cells eliminated across all E : T ratios, revealed striking functional differences among NK cell types (Fig. 4c). This hierarchy was clearly reflected in pooled target-cell killing across the tested E : T ratios (Fig. 4c). exNK cells showed the strongest overall cytotoxic output, eliminating 46.3% of target cells, whereas pbNK killed 20.7%. exNK-asc retained intermediate activity at 26.8%, while pbNK-asc showed only 6.3% target killing. In other words, expanded NK cells killed more than twice as many targets as pbNK and roughly seven times more than pbNK-asc. Thus, ascites conditioning sharply reduced cytotoxic output, but the suppressive effect was far less severe when NK cells had first undergone *ex vivo* expansion.

A similar trend emerged when the analysis was shifted from target-centered outcomes to effector-centered outcomes (Fig. 4d). Analysis of cytotoxic NK cell frequency, defined as the fraction of effectors capable of eliminating at least one target, further differentiated functional states (Fig. 4d). Just over half of exNK cells were cytotoxic overall (51.1%), compared with 36.2% for exNK-asc and 29.2% for pbNK. By contrast, only 11.2% of pbNK-asc cells killed even a single target. The differences became even more pronounced when serial killing was examined (Fig. 4e). Here, serial killing was defined as the ability of a single NK cell to sequentially eliminate more than one target and was assessed exclusively in droplets with E : T ratios of 1 : 2 to 1 : 4. exNK showed the highest serial-killer frequency at 43.8%, meaning that nearly half of expanded NK cells in multi-target droplets eliminated more than one target. exNK-asc still showed detectable serial-killer activity at 20.2%, whereas pbNK reached 12.3%. pbNK-asc was almost completely inactive in this regard, with a serial-killer frequency of just 1.4%. Together, these data indicate that *ex vivo* expansion does not simply increase total killing, but specifically enriches for the most functionally valuable NK-cell subsets.

Time-course analysis further emphasized how strongly NK-cell state influenced cytotoxic kinetics (Fig. 4f–h). exNK cells separated from the other groups early, already reaching 23.4% target killing by 2 h and climbing to 46.3% by 10 h. Their cytotoxic NK-cell fraction rose rapidly as well, from 31.6% at 2 h to just over 51% at the endpoint, while serial-killer frequency increased from about 20.4% to 43.8% over the same period. exNK-asc followed the same general trajectory, but with slower and blunted kinetics, indicating that ascites exposure reduced but did not eliminate cytotoxic activity, ending at 26.8% target killing, 36.2% cytotoxic NK cells, and about 20% serial killers. pbNK showed a weaker intermediate response, whereas pbNK-asc remained largely flat throughout the experiment, with minimal increases in killing, cytotoxic frequency, or serial-killer activity. These kinetics suggest that pbNK-asc cells were not merely delayed, but profoundly suppressed across the full observation window.

To determine how cytotoxic function changed with target burden, we next examined killing across E : T ratios from 1 : 1 to 1 : 4 (Fig. 4i–k). The heatmaps showed that the overall functional hierarchy was preserved across target loads. exNK consistently displayed the strongest activity, with high target killing, high cytotoxic NK-cell frequency, and the most prominent serial-killer phenotype across nearly all E : T ratios. exNK-asc showed a lower but still detectable level of activity across conditions, with its functional profile becoming more evident at higher target loads. pbNK exhibited an intermediate pattern, with modest activity that varied across ratios. In contrast, pbNK-asc remained the weakest condition throughout, showing low target killing, low cytotoxic NK-cell frequency, and minimal serial-killer activity across all E : T ratios.

The supplementary analyses supported these trends without changing the overall interpretation. When all NK groups were pooled, target killing showed only a modest upward trend across E : T ratios (Fig. S7). By comparison, pooled cytotoxic NK-cell frequency increased more noticeably with target number (Fig. S8), likely because droplets containing more targets provide greater opportunity for a functionally competent NK cell to register at least one killing event within the imaging window. Pooled serial-killer frequency also rose at higher target loads, particularly in 1 : 4 droplets (Fig. S9). However, these pooled views masked strong state-dependent differences, with exNK and exNK-asc

Open Access Article. Published on 13 May 2026. Downloaded on 6/3/2026 1:05:32 PM.
This article is licensed under a Creative Commons Attribution 3.0 Unported Licence.

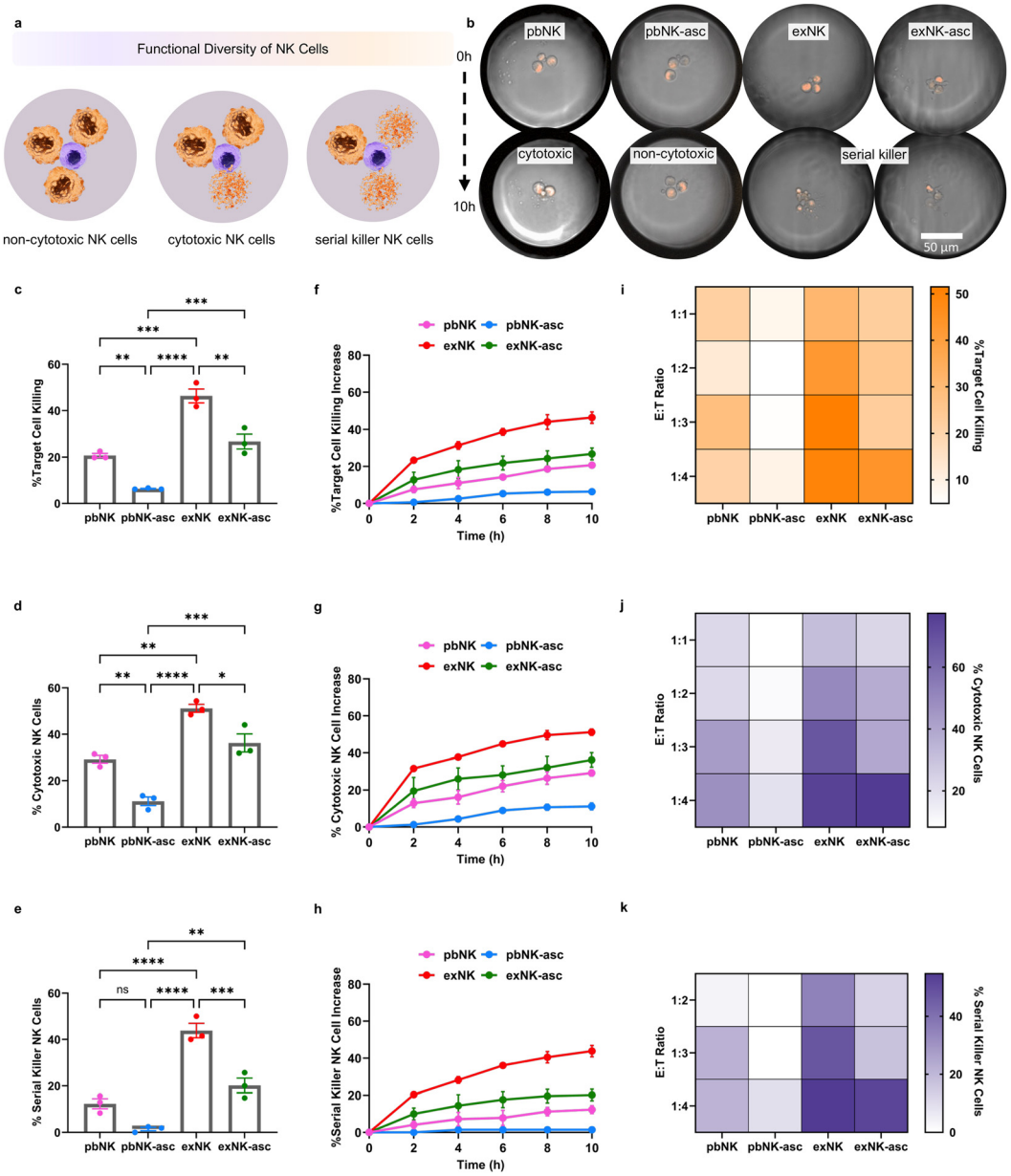

Fig. 4 Functional diversity and cytotoxic activity of NK cell subsets against K562 target cells. (a) Schematic illustrating the functional diversity of NK cells, including non-cytotoxic NK cells, cytotoxic NK cells, and serial-killer NK cells. (b) Representative microscopy images showing NK-cell-mediated killing activity in droplets across different NK-cell types (pbNK, pbNK-asc, exNK, exNK-asc) at 0 h and 10 h time points. Scale bar, 50 μm. (c) Percentage of target-cell killing across NK-cell types, with data pooled across the tested E : T ratios. (d) Percentage of cytotoxic NK cells across NK-cell types, with data pooled across the tested E : T ratios. (e) Percentage of serial-killer NK cells across NK-cell types, with data pooled across the tested E : T ratios. Kinetics of (f) target-cell killing, (g) cytotoxic NK-cell increase, and (h) serial-killer NK-cell increase over 10 h across different NK-cell types, with data pooled across the tested E : T ratios. Heatmaps showing (i) target-cell killing efficiency, (j) cytotoxic NK-cell frequency, and (k) serial-killer NK-cell frequency across varying E : T ratios (1 : 1 to 1 : 4) for each NK-cell type. Data represent three independent biological replicates for each condition (n = 3). The underlying sample sizes for panels (c), (f), and (i) are total target cells. For panels (c) and (f), pooled across the tested E : T ratios: pbNK (n = 390), pbNK-asc (n = 392), exNK (n = 451), and exNK-asc (n = 365). For panel (i), by NK-type/E : T-ratio condition: 1 : 1, pbNK (n = 72), pbNK-asc (n = 76), exNK (n = 71), exNK-asc (n = 56); 1 : 2, pbNK (n = 118), pbNK-asc (n = 118), exNK (n = 148), exNK-asc (n = 96); 1 : 3, pbNK (n = 108), pbNK-asc (n = 114), exNK (n = 156), exNK-asc (n = 153); and 1 : 4, pbNK (n = 92), pbNK-asc (n = 84), exNK (n = 76), exNK-asc (n = 60). The underlying sample sizes for panels (d), (g), and (j) are droplets. For panels (d) and (g), pooled across the tested E : T ratios: pbNK (n = 190), pbNK-asc (n = 194), exNK (n = 216), and exNK-asc (n = 170). For panel (j), by NK-type/E : T-ratio condition: 1 : 1, pbNK (n = 72), pbNK-asc (n = 76), exNK (n = 71), exNK-asc (n = 56); 1 : 2, pbNK (n = 59), pbNK-asc (n = 59), exNK (n = 74), exNK-asc (n = 48); 1 : 3, pbNK (n = 36), pbNK-asc (n = 38), exNK (n = 52), exNK-asc (n = 51); and 1 : 4, pbNK (n = 23), pbNK-asc (n = 21), exNK (n = 19), exNK-asc (n = 15). The underlying sample sizes for panels (e), (h), and (k) are single-NK droplets containing ≥2 target cells. For panels (e) and (h), pooled across the tested E : T ratios: pbNK (n = 118), pbNK-asc (n = 118), exNK (n = 145), and exNK-asc (n = 114). For panel (k), by NK-type/E : T-ratio condition: 1 : 2, pbNK (n = 59), pbNK-asc (n = 59), exNK (n = 74), exNK-asc (n = 48); 1 : 3, pbNK (n = 36), pbNK-asc (n = 38), exNK (n = 52), exNK-asc (n = 51); and 1 : 4, pbNK (n = 23), pbNK-asc (n = 21), exNK (n = 19), exNK-asc (n = 15). Asterisks represent ns ($p > 0.05$), * ($p \leq 0.05$), ** ($p \leq 0.01$), *** ($p \leq 0.001$), and **** ($p \leq 0.0001$) from one-way or two-way ANOVA with Tukey's multiple comparisons test. Error bars represent SEM.

This journal is © The Royal Society of Chemistry 2026

Open Access Article. Published on 13 May 2026. Downloaded on 6/3/2026 1:05:32 PM.
This article is licensed under a Creative Commons Attribution 3.0 Unported Licence.

accounting for most of the higher-function behavior at elevated target density.

Because each droplet contained a single NK cell, we next examined the distribution of per-NK kill fraction to resolve within-group functional heterogeneity (Fig. S10). This analysis again showed a clear functional hierarchy. pbNK-asc was dominated by non-functional cells, with 89.2% of droplets showing no killing at all, whereas exNK had the highest mean kill fraction (0.419) and the largest fraction of complete killers. pbNK showed an intermediate distribution,

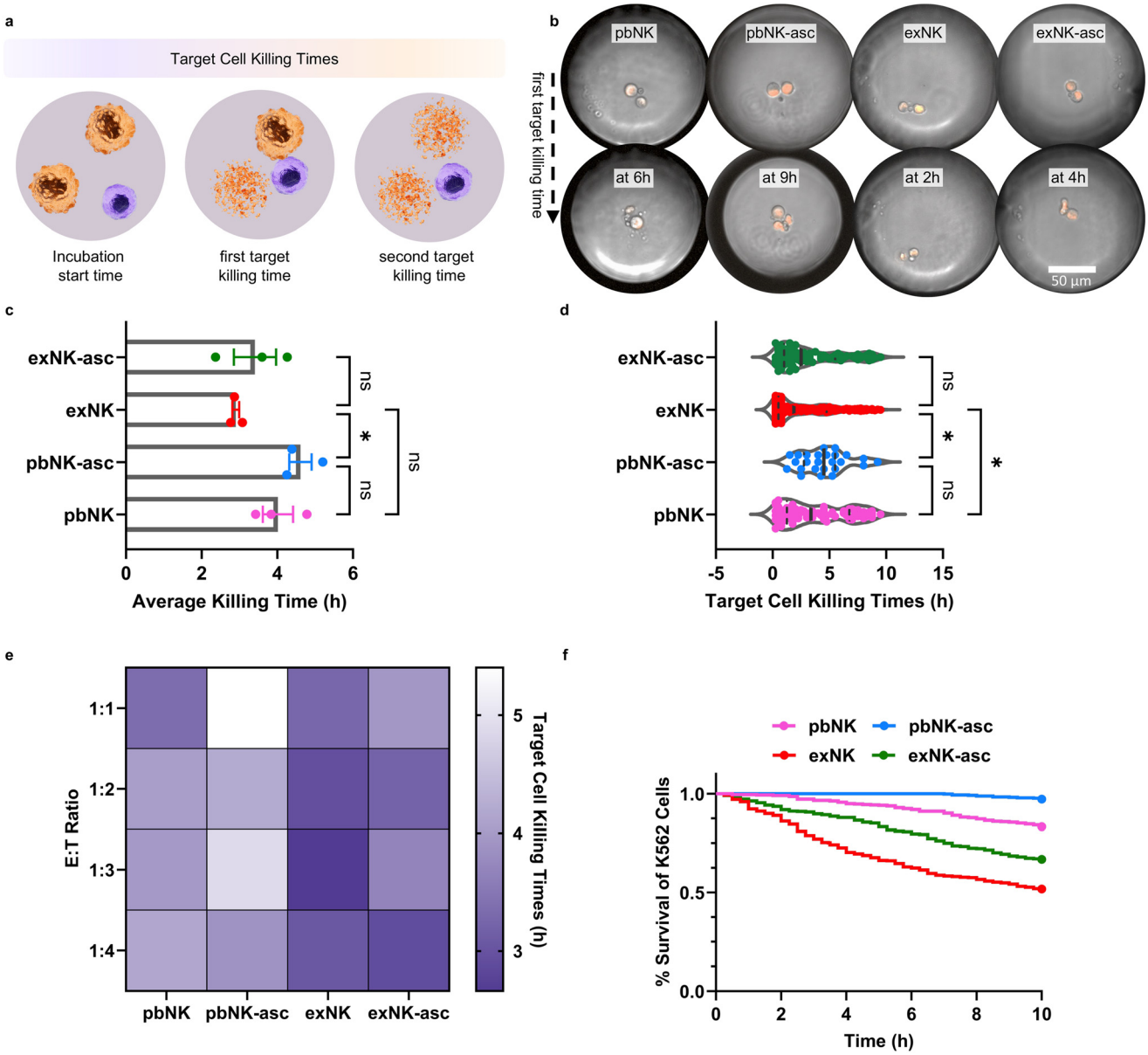

Fig. 5 Kinetics of target cell killing by NK cell subsets. (a) Schematic illustrating NK-cell-mediated killing events at different time points, showing incubation start time, first target killing time, and second target killing time. (b) Representative microscopy images showing the first target-cell killing event in droplets containing different NK-cell types at the indicated time points. Scale bar, 50 μm. (c) Comparison of average target-cell killing times among NK-cell subsets (pbNK, pbNK-asc, exNK, exNK-asc). (d) Distribution of individual target-cell killing times across different NK-cell types. Data in panel (c) represent three independent biological replicates for each condition (n = 3). The underlying sample size for panels (c) and (d) is the number of kill events pooled across the tested E : T ratios: pbNK (n = 82), pbNK-asc (n = 25), exNK (n = 204), and exNK-asc (n = 95). (e) Heatmap showing average target-cell killing times across varying effector-to-target (E : T) ratios (1 : 1 to 1 : 4) for each NK-cell type. The underlying sample size for panel (e) is the number of kill events in each NK-cell-type/E : T-ratio condition: 1 : 1, pbNK (n = 15), pbNK-asc (n = 5), exNK (n = 22), exNK-asc (n = 12); 1 : 2, pbNK (n = 15), pbNK-asc (n = 6), exNK (n = 65), exNK-asc (n = 23); 1 : 3, pbNK (n = 31), pbNK-asc (n = 6), exNK (n = 80), exNK-asc (n = 34); and 1 : 4, pbNK (n = 21), pbNK-asc (n = 8), exNK (n = 37), exNK-asc (n = 26). (f) Survival kinetics of K562 target cells over time when co-encapsulated with different NK-cell types. The underlying sample size for panel (f) is total target cells pooled across the tested E : T ratios: pbNK (n = 390), pbNK-asc (n = 392), exNK (n = 451), and exNK-asc (n = 365). For panels (c) and (d), asterisks represent ns ($p >$ 0.05), * ($p \leq 0.05$), ** ($p \leq 0.01$), and *** ($p \leq 0.001$) from one-way ANOVA with Tukey's multiple comparisons test. Error bars represent SEM.

Open Access Article. Published on 13 May 2026. Downloaded on 6/3/2026 1:05:32 PM.
This article is licensed under a Creative Commons Attribution 3.0 Unported Licence.

while exNK-asc also retained appreciable functional heterogeneity and remained clearly distinct from the profoundly impaired pbNK-asc state. Stratification by initial target number showed that the same pattern persisted across target loads, with the strongest separation between groups becoming especially apparent in droplets containing three or four initial targets.

Together, these data establish a robust functional hierarchy among the four NK-cell states. *Ex vivo* expansion increased not only overall target killing, but also the fraction of cytotoxic cells, the prevalence of serial killers, and the speed with which these behaviors emerged. Ascites exposure suppressed every functional metric measured here, but expanded NK cells retained substantially more activity than freshly isolated pbNK cells exposed to the same suppressive environment. Across pooled analyses, E : T-specific analyses, and single-cell kill-fraction distributions, the same conclusion remained consistent: exNK represented the most functionally competent state, pbNK-asc the most impaired, and exNK-asc a partially preserved intermediate phenotype with clear therapeutic promise in immunosuppressive environments.

2.5. Expanded NK cells kill more rapidly, whereas TME-exposed NK cells display slower cytotoxicity

Killing kinetics, the time interval from effector-target engagement to target cell death, directly determines the throughput capacity of individual NK cells in therapeutic settings.[44] Rapid cytotoxic responses enable NK cells to sequentially engage multiple targets before tumor escape mechanisms activate, while prolonged killing times reduce overall anti-tumor efficacy and may permit adaptive resistance.[45] In heterogeneous tumor microenvironments where both effector quality and target density vary spatially, killing speed becomes a critical determinant of local tumor control.[46] Traditional endpoint assays measure cumulative lysis without resolving the temporal dynamics of individual killing events, obscuring differences in effector kinetics that may predict clinical outcomes. Single-cell temporal profiling is therefore essential for identifying NK cell products capable of rapid, sustained cytotoxic responses under therapeutic conditions.

To examine cytotoxic timing at single-cell resolution, we quantified the time of each accepted target-death event (Fig. 5a). The schematic illustrates the temporal sequence of NK cell-mediated cytotoxicity, from initial incubation through first and second target killing events, capturing both single-hit and serial killing dynamics. Representative microscopy images document the progression of target elimination at varying time points across different NK cell groups (Fig. 5b). These images reveal striking differences in killing speed: exNK and exNK-asc droplets show target cell death within early time frames, whereas pbNK and pbNK-asc droplets exhibit prolonged target survival with delayed or absent death events.

When replicate-level average killing times were compared across NK-cell states (Fig. 5c), exNK showed the shortest mean killing time (2.9 h), whereas pbNK-asc showed the longest (4.6 h). pbNK (4.0 h) and exNK-asc (3.4 h) fell between these values. However, only the exNK *versus* pbNK-asc comparison reached statistical significance, indicating that the average killing-time readout distinguishes these two groups most clearly, while the other conditions remain partially overlapping. Analysis of individual killing events (Fig. 5d) supported this more restrained interpretation. exNK killing events were shifted toward earlier time points, with a median killing time of 1.9 h, compared with 3.4 h for pbNK and 4.5 h for pbNK-asc. In this event-level comparison, exNK differed significantly from both pbNK groups. exNK-asc showed an intermediate distribution with a median of 2.5 h.

The heatmap in Fig. 5e extends this analysis across E : T ratios and shows that killing-time behavior was not driven by a simple target-number effect. exNK generally occupied the lower killing-time range across the tested droplet types, while pbNK-asc tended to appear in the higher range when killing events were present. At the same time, the pattern was not uniform across every ratio, and the values overlapped considerably among groups. Consistent with this, the ratio-stratified comparisons in Fig. S11 showed that most pairwise comparisons within a given E : T ratio were not significant, with only isolated significant differences (Fig. S11). When all NK-cell groups were pooled by droplet type, average killing times remained broadly similar across 1 : 1 to 1 : 4 droplets (Fig. S12). Together, these data suggest that within the tested range, NK-cell state contributed more to variation in killing time than E : T ratio, but that this effect was modest rather than absolute.

Survival kinetics of K562 targets provided an integrated view of cumulative cytotoxic activity over time (Fig. 5f). The survival curves separated early and remained distinct throughout the assay. exNK produced the steepest decline in target survival, dropping to 81.8% at 1 h, 69.4% at 4 h, and 54.8% at 10 h, corresponding to the greatest cumulative target loss. In contrast, pbNK-asc showed only a minimal decline, with survival remaining at 100% through 1 h, 97.2% at 4 h, and 93.6% at 10 h, consistent with markedly impaired cytotoxic progression. pbNK and exNK-asc both showed progressive decreases in K562 survival over time, with exNK-asc consistently producing somewhat greater cumulative target depletion than pbNK, culminating in 74.0% *versus* 79.0% survival at 10 h. These patterns show that expansion was associated with more rapid and sustained cumulative target-cell loss, while ascites exposure shifted survival upward in both NK-cell backgrounds, indicating reduced overall killing. Notably, although ascites suppressed expanded NK cells as well, exNK-asc still showed greater cumulative target depletion than pbNK-asc and, numerically, pbNK by the end of the assay, suggesting partial retention of cytotoxic function after expansion.

This journal is © The Royal Society of Chemistry 2026

Open Access Article. Published on 13 May 2026. Downloaded on 6/3/2026 1:05:32 PM. This article is licensed under a Creative Commons Attribution 3.0 Unported Licence.

3. Discussion

NK cell immunotherapy has emerged as a promising approach in cancer treatment due to the innate cytotoxic capabilities of NK cells, which allow them to identify and destroy cancer cells without prior sensitization.[47] Accurate assessment of immune cell cytotoxicity is crucial for advancing NK cell-based therapies. Traditional methods, such as the Cr-51 and flow cytometry-based tests, have provided foundational insights but are limited by their inability to offer individual cell analysis and real-time monitoring.[10] In this study, we developed a droplet-based microfluidic cytotoxicity assay that enables single-cell investigation of NK cell-mediated cytotoxicity by generating time-resolved, per-droplet functional trajectories and providing real-time insight into NK cell interactions with cancer cells at scale. Although prior droplet-based NK studies have already demonstrated single-cell functional profiling, serial killing, and in some cases automated fluorescence-based droplet analysis, the present study does not claim the first droplet-based NK single-cell assay. Rather, its key technical contribution is the integration of machine-learning-based, frame-wise K562 target detection with a deterministic temporal event-calling algorithm that standardizes death-event identification across full 10-hour time-lapse sequences, while its key biological contribution is the matched-donor comparison of pbNK, pbNK-asc, exNK, and exNK-asc states within the same analytical framework. This combination enables reproducible quantification of heterogeneous behaviors such as contact outcomes, serial killing, and killing-time distributions across clinically relevant NK states using a matched-donor design. Standardizing these readouts at the per-droplet level reduces observer dependence and increases throughput, enabling robust estimates of fraction killed, time-to-death distributions, and serial killing across donors and conditions. In addition, comparison of the automated analysis with blinded manual analysis showed strong agreement for target killing, cytotoxic NK-cell frequency, serial killer frequency, and killing time (Fig. S6). This platform offers significant advantages over traditional bulk cytotoxicity assays by enabling precise, time-resolved, single-cell analysis and addressing critical limitations such as lack of real-time monitoring and inability to capture functional heterogeneity within NK cell populations.[23,25,26,28]

NK behavior in E:T droplets resolved into three outcome classes: no contact, contact without lysis, and contact culminating in lysis. Conditioning modulates both the probability of contact formation and the conditional probability that a contact proceeds to killing. *Ex vivo* expansion increases both parameters, whereas exposure to ascites-derived soluble factors reduces them. Cytotoxic output can be conceptualized as the product P (contact) × P (kill|contact). Contact is necessary but not sufficient for lysis; progression to killing likely reflects synapse quality, receptor signaling sufficiency, and effective granule polarization and release.[34] Increases in target density primarily elevate opportunities for contact rather than the per-contact execution probability, which explains modest reductions in no-contact events without a proportional rise in killing efficiency. Furthermore, time-lapse sequences of sequential killing showed that an NK cell could engage a second target either after detaching from a previously killed cell or while maintaining continuous or near-continuous contact, indicating that serial killing does not require a single obligate detachment-and-reengagement sequence. Together, these observations emphasize the importance of productive and sustained target engagement for effective target cell killing.

The findings from this study provided significant insights into the functionality of NK cells under various conditions and underlined the potential of NK cell-based immunotherapies (Fig. S13 and Movie S3). exNK cells demonstrated the highest cytotoxic activity, including the fastest killing times, the highest killing efficiency, and notable serial killing activity. These findings align with prior studies showing that expansion processes enhance NK cell functionality and anti-tumor activity by improving their cytotoxic potential and proliferative capacity.[6–8] This robustness positions them as strong candidates for developing NK cell-based treatments for cancer.

Conversely, pbNK-asc cells exhibited significantly reduced functionality, with minimal cytotoxic activity and no serial killing events observed. These cells also showed delayed killing times. This reflects the profound negative effects of suppression conditions, such as exposure to the ascites TME. This aligns with previous research indicating that factors within the TME, such as ascitic fluid, can impair NK cell recognition and killing abilities.[4,5] Overcoming these inhibitory effects remains a critical challenge in improving NK cell therapies for tumors.

Interestingly, exNK-asc cells, which were exposed to suppressive conditions following expansion, retained a significant degree of cytotoxic activity and serial killing capacity. Although their performance was lower than that of exNK cells, it was still markedly higher than that of pbNK-asc cells. This suggests that while suppression following expansion diminishes NK cell function, it does not completely negate the benefits gained through the expansion process.[48] These findings highlight the potential for combining NK cell expansion strategies with supportive treatments to counteract the suppressive effects of the TME.

A critical methodological strength of this study is the use of primary peripheral blood NK cells rather than immortalized NK-92 cell lines, which are commonly employed in preclinical cytotoxicity assays. While NK-92 cells offer experimental convenience through unlimited expansion and standardized phenotypes, they lack the full repertoire of activating and inhibitory receptors expressed by primary NK cells and exhibit distinct metabolic profiles that may not accurately predict clinical responses.[49] Primary NK cells better recapitulate the functional heterogeneity and receptor diversity found in therapeutic NK cell products, providing

Open Access Article. Published on 13 May 2026. Downloaded on 6/3/2026 1:05:32 PM.
This article is licensed under a Creative Commons Attribution 3.0 Unported Licence.

more clinically relevant insights into how conditioning regimens modulate effector function. Furthermore, our experimental design derives all four NK cell states (pbNK, pbNK-asc, exNK, exNK-asc) from identical donor samples across three independent biological replicates, eliminating inter-donor genetic variability as a confounding factor. This matched-donor approach enables direct attribution of functional differences to conditioning protocols rather than baseline donor heterogeneity, which is particularly important given that NK cell repertoires vary substantially across individuals due to polymorphisms in killer immunoglobulin-like receptor (KIR) genes and their HLA class I ligands.[9,50] By controlling for donor variability while systematically varying conditioning regimens, this design provides robust evidence that *ex vivo* expansion and TME exposure directly modulate NK cell functional capacity in therapeutically relevant contexts.

Our findings should be interpreted in the context of the study design. We used K562 as a standardized target throughout, which facilitates controlled comparisons across NK states and E : T ratios but does not capture the antigen profiles, adhesion properties, or resistance mechanisms of other tumor types. NK-side annotations relied on manual, morphology-based scoring of viable effectors and interaction outcomes. Although these criteria were supported by FVS520 live/dead staining outside droplets and by single-cell droplet controls showing minimal spontaneous NK-cell death over the imaging window, we did not directly validate NK viability using FVS520 or another live/dead marker under droplet-confined co-culture conditions. This is a limitation because NK cells can undergo transient deformation during prolonged target engagement, and morphology alone may not fully distinguish interaction-associated shape changes from loss of viability.

Misclassification of NK viability could affect downstream NK-normalized metrics, including cytotoxic NK-cell frequency, serial-killer frequency, and attachment outcome categories. For example, false assignment of a non-viable NK cell as viable would increase the denominator of viable effectors and could underestimate the fraction of cytotoxic or serial-killer NK cells, whereas erroneous exclusion of viable but deformed NK cells could reduce the denominator and potentially overestimate activity among the retained viable population. Since the same conservative criteria were applied across all NK-cell states, any residual misclassification is expected to have a greater effect on absolute NK-normalized values than on the relative functional hierarchy observed among conditions. Future implementations could incorporate in-droplet NK viability reporters or automated NK segmentation to further reduce this source of uncertainty.

In addition, the droplet assay evaluates contact-mediated cytotoxicity in suspension, without a three-dimensional matrix or scaffold, so matrix-dependent processes such as integrin engagement, mechanotransduction, and migration in confined spaces are not represented. Together, these considerations bound the generalizability of the work and indicate that broader target panels, automated NK detection, and matrix-integrated formats would further strengthen the conclusions.

4. Experimental section

Cell culture

K562 target cells. K562 cells stably expressing mKate2 (genetically engineered in the Ashkar Lab) were maintained in RPMI-1640 (ATCC 30-2001™) supplemented with 10% FBS (ATCC 30-2000™), 1% penicillin–streptomycin (Sigma-Aldrich), and 0.1% Plasmocin™ (InvivoGen). Cells were cultured at 37 °C, 5% CO_2 in a humidified incubator, passaged approximately every 2 days, and harvested at ~1 × 10^6 viable cells per mL.

NK cell isolation and culture. Peripheral blood NK cells were isolated from fresh blood of three female donors using a commercial human NK Cell Isolation Kit (negative selection; Miltenyi Biotec, Germany; Cat. 130-092-657) according to the manufacturer's protocol. NK-cell purity was confirmed by flow cytometry using the following antibodies (BD Biosciences): anti-human CD45 (clone HI30, purified; Cat. 555480), CD56 (clone MY31, PE; Cat. 556647), and CD3 (clone OKT3, PE; Cat. 566684). Staining was performed at the manufacturer-recommended concentrations for 20 min at room temperature, protected from light, followed by standard washes. Isolated NK cells were cultured in RPMI-1640 (ATCC 30-2001™) with 10% FBS (ATCC 30-2000™), 1% penicillin–streptomycin (Sigma-Aldrich), 0.1% Plasmocin™ (InvivoGen), and 50 ng mL^{-1} recombinant human IL-2 (Proleukin®, Novartis/Clinigen).

Conditioning and expansion. Freshly isolated pbNK cells were used immediately for assays or reserved for subsequent treatments. To generate pbNK-asc, pbNK cells were cultured for 3 days in cell-free malignant ascites collected under sterile conditions from multiple ovarian-cancer patients; samples were not pooled and were used separately on a per-patient basis. Ascites was centrifuged at 300 g for 10 minutes to remove debris before use. For exNK cells, pbNK cells were expanded by co-culture for 3 weeks with irradiated (100 Gy) K562-mbIL-21 feeder cells (Clone 9, gift from Dr. Dean A. Lee's lab), replenished weekly (days 0, 7, 14) at a 1 : 2 NK : feeder ratio, maintaining NK density at 5 × 10^5 cells per mL post-replenishment, with media changes every 2–3 days (max 72 h) in NK culture medium (as described above) containing 50 ng mL^{-1} recombinant human IL-2 (rhIL-2) (Proleukin®, Novartis/Clinigen), at 37 °C and 5% CO_2 in T25/T75 flasks. exNK-asc cells were obtained by culturing exNK in patient ascites for an additional 3 days.

All blood draws, NK cell isolation, culturing, and preparation were performed by the Ashkar Lab (McMaster University, Hamilton, ON, Canada). All procedures were approved by the Institutional Biosafety Committee (BUP#146) and the McMaster Research Ethics Board (REB#15552), with written informed consent from all human participants.

This journal is © The Royal Society of Chemistry 2026

Open Access Article. Published on 13 May 2026. Downloaded on 6/3/2026 1:05:32 PM. This article is licensed under a Creative Commons Attribution 3.0 Unported Licence.

Droplet-based microfluidic NK cytotoxicity assay

A commercial droplet generation and storage chip (Fluidic 719, microfluidic ChipShop) was utilized for the assay. The device was fabricated in polycarbonate (PC; chip body: mcs-PC 13) with a 175 μm PC lid (mcs-foil 042; Tg 145 °C) and used as received without additional surface coating. The architectural design includes a flow-focusing junction. Channel dimensions are region-dependent to optimize droplet formation and stability. The channel widths range from a minimum of 82 μm at the nozzle to 120–161 μm in the adjacent junction sections, and reach 161 μm in the main transport channels leading to the storage array. The channel depth is strategically region-dependent, measuring 50 μm at the narrowest junction section, 100–115 μm in the adjacent junction channels, and 100 μm in the downstream storage array. The chip features 2261 microfluidic storage positions, each with a diameter of 173 μm.

Droplet formation was performed using a Fluigent Flow EZ™ pressure-driven platform. To generate monodisperse, aqueous droplets, the continuous phase, consisting of dSURF oil (2% fluorosurfactant in Novec™ 7500), was maintained at a constant flow rate of 15 μL min^{-1}. The dispersed phase was introduced through two separate aqueous inlets (target and effector cells), each set to a constant 2 μL min^{-1} for a total aqueous flow of 4 μL min^{-1}. These parameters consistently yielded monodisperse droplets with a diameter of 176.4 ± 3.9 μm (mean ± SD; n = 24), which falls within the suggested range of 150–180 μm for this chip architecture. Because the droplet diameter is larger than the 100 μm trap depth, the droplets adopt a slightly flattened ("pancaked") morphology between the top and bottom of the channel. This specifically engineered confinement increases surface contact within the 173 μm traps, preventing droplet drift and maintaining a consistent focal plane for high-resolution optical observation.

Trapped droplet volume calculation based on channel confinement:

Measured trapped droplet diameter: d = 176.4 μm (mean; n = 24); trap depth: h = 100 μm

Cylindrical approximation: $V \approx \pi(d/2)^2 h$

$$V \approx \pi(88.2\ \mu m)^2(100\ \mu m) \approx 2.44 \times 10^6\ \mu m^3 \approx 2.44\ nL$$

Propagating diameter variability: $V \propto d^2$

$$V \approx 2.44 \pm 0.11\ nL\ (\text{mean} \pm \text{SD}; n = 24)$$

To achieve the desired pairing efficiency, input concentrations were calculated based on Poisson distribution statistics for the effective droplet volume. NK cells (2×10^5 cells per mL) and mKate2-expressing K562 target cells (1×10^6 cells per mL) were introduced through separate aqueous inlets to enable co-encapsulation.

Effective in-droplet concentrations and expected occupancy:

Equal aqueous inlet flow rates (2 μL min^{-1} each; total Q_{aq} = 4 μL min^{-1}) give 1 : 1 mixing of the two streams.

$$C_{K562,eff} = (1 \times 10^6)(2/4) = 5 \times 10^5\ \text{cells per mL}$$

$$C_{NK,eff} = (2 \times 10^5)(2/4) = 1 \times 10^5\ \text{cells per mL}$$

Droplet volume for Poisson loading: $V \approx 2.44$ nL $= 2.44 \times 10^{-6}$ mL

Expected mean occupancy per droplet: $\lambda = C{\cdot}V$

$$\lambda_{K562} = (5 \times 10^5)(2.44 \times 10^{-6}) = 1.22\ \text{target cells per droplet}$$

$$\lambda_{NK} = (1 \times 10^5)(2.44 \times 10^{-6}) = 0.244\ \text{NK cells per droplet}$$

Throughout all experiments, the flow rates, droplet size, and generation frequency were strictly maintained at constant values to ensure the physical environment remained identical for every droplet. Consequently, the observed range of effector-to-target (E : T) ratios (1 : 1 to 1 : 4) resulted solely from the stochastic nature of encapsulation at these fixed concentrations. Droplet occupancy was determined at the first timepoint and only droplets containing one NK cell paired with one to four K562 cells were included in downstream analyses.

Following encapsulation, chips were incubated at 37 °C and 5% CO_2 in a humidified atmosphere. Time-lapse imaging was performed on a Nikon Eclipse Ti2-E inverted microscope using NIS-Elements ND acquisition at 10× magnification. Images were collected at 15-minute intervals over a total duration of 10 hours to monitor the dynamic NK-target cell interactions within the trapped droplets.

Semi-automated image analysis

The final analysis workflow used in this study consisted of three sequential computational stages. First, raw time-lapse microscopy images were processed by a YOLOv8-based detection and tracking module to identify droplets and K562 target cells in each frame and to export per-droplet cell-count trajectories. Second, these trajectories were analyzed using Constrained Decline Analysis v3 (CDA3) to estimate droplet-level death counts and killing times. Third, per-experiment outputs were aggregated into summary tables and figure-

Open Access Article. Published on 13 May 2026. Downloaded on 6/3/2026 1:05:32 PM.
This article is licensed under a Creative Commons Attribution 3.0 Unported Licence.

ready datasets for downstream statistical analysis. The final quantitative outputs used in the manuscript were taken from the processed-result files generated by this temporal event-calling algorithm, whereas earlier pipeline versions were retained only as legacy analyses and were not used for the final study. The workflow also supported generation of frame-level overlay images, including raw-frame copies, droplet-ID overlays, and droplet-ID-plus-cell overlays, to facilitate quality control and blinded manual review. Droplet-ID tracking images without cell tracking overlays were used for all manual analyses to facilitate blinded manual review and match droplet IDs with the automated analysis.

For automated detection, brightfield-TRITC overlay images of droplet arrays (2048 × 2044 pixels) were annotated in Roboflow with bounding boxes for three manually labeled classes: droplets, viable K562 cells and dead K562 cells. The annotation set comprised 198 source images and 3675 total annotations, including 1343 droplets, 1764 viable K562 cells and 568 dead K562 cells. Source images were split 92/4/4% into training, validation, and test sets, tiled at high resolution, and augmented on the training set only using the Roboflow pipeline, including horizontal and vertical flips, rotation, brightness adjustment, and blur perturbations. This yielded 4266 augmented training images, 180 validation images, and 180 test images. Training was performed for 50 epochs using the Roboflow 3.0 Object Detection (Accurate) architecture, and checkpoint 4 was selected as the best-performing model based on validation performance. The final detector achieved a validation mAP@50 of 90.9%, with per-class AP values of 97% for droplets, 97% for viable K562 cells, and 79% for dead K562 cells; performance on the held-out test set was 85.8% precision and 91.3% recall. Trained weights were exported in PyTorch format and used for inference through the Ultralytics YOLOv8 library.

During inference, all 41 frames from each 10 h time-lapse sequence, acquired at 15 min intervals, were processed rather than relying on endpoint images alone. To maximize frame-level recall, class-specific confidence thresholds were intentionally set below the training optimum: 20% for droplets, 2.5% for viable K562 cells, and 3.0% for dead K562 cells, with non-maximum suppression applied at 25% IoU. K562 detections were assigned to droplets by geometric containment of the cell center within the droplet boundary, and droplets were linked across frames by nearest-neighbor matching of droplet centroids using a 75-pixel Euclidean-distance threshold. When overlapping bounding boxes classified the same cell as both alive and dead within a frame, the dead label was retained when overlap exceeded 35% IoU, thereby enforcing a monotonic alive-to-dead transition. For each droplet in each frame, the pipeline exported total, alive, and dead K562 counts to CSV for downstream temporal analysis.

Droplet-level killing trajectories were analyzed using a deterministic temporal event-calling algorithm that estimated droplet-level death counts and killing times from frame-wise alive-cell trajectories. For single-target droplets, death timing was assigned using a hierarchical fallback strategy to preserve event timing when the primary estimate was ambiguous. Specifically, timing was assigned from the first frame at which the smoothed alive signal fell below 0.5, the frame of maximum decline, or the midpoint of the detected decline region. For multi-target droplets, late-stage baseline estimation was made adaptive to signal variability to reduce false decline estimates arising from transient YOLO tracking loss. The first death event was identified within a constrained local decline window to preserve first-death accuracy, whereas subsequent deaths were detected across the remaining trajectory using a sustained-decline rule. Later events required a decrease of at least 0.4 in the alive-cell signal that persisted for 5 consecutive frames without substantial rebound, using a recovery tolerance of 0.15. Additional analysis parameters included a 5-frame smoothing window, early and late trajectory fractions of 0.10 and 0.25, a minimum spacing of 0.50 h between death calls, a frame interval of 0.25 h, and a percentile-based robust estimate of initial target number using the 75th percentile of observed cell counts.

The temporal event-calling algorithm was run in batch across all experiments using the exported tracking CSVs from step 1. Raw image folders were first converted into per-droplet tracking outputs, the temporal event-calling algorithm was then applied to count death events and assign death times, and summary scripts subsequently assembled experiment-level and graph-level outputs. The final processed-result files contained automated death counts, killing times, and manual-annotation columns side by side, enabling direct comparison between automated and manual analyses. Figure source data were exported as Prism-compatible CSV files. Analysis was restricted to droplets containing exactly one NK cell and one to four K562 target cells at the first time point, whereas droplets containing clusters of five or more target cells were excluded from the final quantitative dataset.

In-droplet NK-cell enumeration, viability scoring, and NK-K562 attachment annotation were performed by blinded observers using standardized criteria rather than by the deployed detector. NK cells were identified using the combined features of absent TRITC signal, smaller size relative to K562 cells, brightfield morphology, and positional continuity across adjacent frames, so that the same cell could still be followed during transient deformation at the immunological synapse. Viable NK cells were scored as intact, rounded, TRITC-negative cells with preserved membrane morphology, whereas non-viable NK cells showed condensed or fragmented morphology and were excluded from E:T assignment. Attachment was defined as visible membrane contact or immediate adjacency between an NK cell and a K562 cell that persisted for at least three consecutive frames. Inter-observer agreement for NK cell annotation was verified on a subset of 50 droplets and exceeded Cohen's kappa of 0.90.

This journal is © The Royal Society of Chemistry 2026

Open Access Article. Published on 13 May 2026. Downloaded on 6/3/2026 1:05:32 PM. This article is licensed under a Creative Commons Attribution 3.0 Unported Licence.

To benchmark automated performance, the temporal event-calling algorithm was validated against expert-derived annotations on a subset of 772 annotated droplets using the dedicated validation script included in the Data folder. Validation quantified both death-count accuracy and timing accuracy relative to expert-annotated ground truth, including first-death bias, first-death mean absolute error, the proportion of calls within 1 h of the manual label, and the spread of serial-killing times. This validation framework was used to confirm that the final implementation improved temporal calling relative to earlier pipeline versions while preserving the biological ranking of cytotoxicity across NK-cell groups. In addition, comparison of manual and automated outputs across the main assay metrics, including target-cell killing, cytotoxic NK frequency, serial-killer frequency, and average killing time, showed no significant differences in paired comparisons across the four NK-cell groups.

Validation of morphology-based NK viability scoring. To validate morphology-based NK viability calls derived from brightfield imaging, an orthogonal live/dead assay was performed on a subset of 201 NK cells using the fixable viability dye FVS520. Brightfield-only morphology calls were matched to paired fluorescence readouts. NK cells were divided into live and dead controls; the dead control was generated by thermal killing at 65–70 °C for 5 min. Live and dead cells were mixed 1 : 1 to obtain a population containing both viable and non-viable cells. The mixed cells were washed with PBS, then stained with FVS520 at 1 : 1000 dilution (1 μL dye per 1 mL PBS) for 20 min on ice, protected from light. Cells were washed with PBS and resuspended in NK culture medium, then imaged by brightfield and FITC fluorescence. Morphology-based viability scoring was performed using the brightfield images only, and each per-cell morphology call was matched to the corresponding FVS520 dye status in the paired fluorescence overlay (FVS520− = live; FVS520+ = dead). Agreement between morphology-based scoring and FVS520 status was quantified using a confusion matrix and derived performance metrics (accuracy, sensitivity, specificity, PPV, and NPV).

Statistical Analysis

Error bars on graphs represent SEM. The number of samples for each experiment is specified in figure captions, and the minimum sample size used in this study is three. Graphs were analyzed by a one-way or two-way ANOVA followed by Tukey's multiple comparison test. GraphPad Prism version 10 software (San Diego, CA, USA) was used for statistical analysis and graphs.

Author contributions

R. S. O.: conceptualization, methodology, software, validation, investigation, formal analysis, data curation, visualization, writing – original draft, writing – review & editing. F. V.: conceptualization, methodology, investigation, resources, writing – review & editing. S. N.: methodology and investigation. A. A. A.: conceptualization, supervision, resources, funding acquisition, writing – review & editing. T. F. D.: conceptualization, supervision, resources, project administration, funding acquisition, writing – review & editing. All authors have read and approved the final manuscript.

Conflicts of interest

The authors declare no conflict of interest.

Data availability

Data and code for this article, including the supplementary information (SI), Movies S1–S3, and analysis package, comprising analysis code, model weights, sample input data and intermediate tracking outputs, raw results, processed experiment-level results, figure-source CSVs, validation material, and README files for the data and code, are available in Zenodo at https://doi.org/10.5281/zenodo.20042948.

Acknowledgements

This research was undertaken thanks to the Canada Research Chairs Program awards to T. F. Didar. T. F. Didar is funded by the Natural Sciences and Engineering Research Council of Canada (NSERC) through the Canada Discovery Grant and the Ontario Early Researcher Award. T. F. Didar is also the recipient of the NSERC Aurther B McDonald Fellowship. A. A. Ashkar is a holder of tier 1 Canada Research Chair. This work was supported by a Canadian Institutes of Health Research (CIHR) grant (#20009360) to A. A. Ashkar.

References

1 E. Vivier, E. Tomasello, M. Baratin, T. Walzer and S. Ugolini, *Nat. Immunol.*, 2008, **9**, 503–510.
2 A. G. Freud, B. L. Mundy-Bosse, J. Yu and M. A. Caligiuri, *Immunity*, 2017, **47**, 820–833.
3 N. Shimasaki, A. Jain and D. Campana, *Nat. Rev. Drug Discovery*, 2020, **19**, 200–218.
4 T. Nham, S. M. Poznanski, I. Y. Fan, M. M. Shenouda, M. V. Chew, A. J. Lee, F. Vahedi, Y. Karimi, M. Butcher, D. A. Lee, H. Hirte and A. A. Ashkar, *Cancer Immunol., Immunother.*, 2018, **67**, 575–587.
5 S. M. Poznanski, K. Singh, T. M. Ritchie, J. A. Aguiar, I. Y. Fan, A. L. Portillo, E. A. Rojas, F. Vahedi, A. El-Sayes, S. Xing, M. Butcher, Y. Lu, A. C. Doxey, J. D. Schertzer, H. W. Hirte and A. A. Ashkar, *Cell Metab.*, 2021, **33**, 1205–1220. e5.
6 M. M. Shenouda, A. Gillgrass, T. Nham, R. Hogg, A. J. Lee, M. V. Chew, M. Shafaei, C. Aarts, D. A. Lee, J. Hassell, A. Bane, S. Dhesy-Thind and A. A. Ashkar, *Breast Cancer Res.*, 2017, **19**, 76.

Open Access Article. Published on 13 May 2026. Downloaded on 6/3/2026 1:05:32 PM. This article is licensed under a Creative Commons Attribution 3.0 Unported Licence.

7 F. Vahedi, T. Nham, S. M. Poznanski, M. V. Chew, M. M. Shenouda, D. Lee and A. A. Ashkar, *Sci. Rep.*, 2017, **7**, 12083.
8 S. M. Poznanski, T. M. Ritchie, I. Y. Fan, A. El-Sayes, A. L. Portillo, R. Ben-Avi, E. A. Rojas, M. V. Chew, Y. Shargall and A. A. Ashkar, *J. Immunother. Cancer*, 2021, **9**, e001933.
9 A. Horowitz, D. M. Strauss-Albee, M. Leipold, J. Kubo, N. Nemat-Gorgani, O. C. Dogan, C. L. Dekker, S. Mackey, H. Maecker, G. E. Swan, M. M. Davis, P. J. Norman, L. A. Guethlein, M. Desai, P. Parham and C. A. Blish, *Sci. Transl. Med.*, 2013, **5**, 208ra145.
10 S. Kiesgen, J. C. Messinger, N. K. Chintala, Z. Tano and P. S. Adusumilli, *Nat. Protoc.*, 2021, **16**, 1331–1342.
11 A. M. Foudeh, T. F. Didar, T. Veres and M. Tabrizian, *Lab Chip*, 2012, **12**, 3249–3266.
12 A. Shakeri, S. Khan and T. F. Didar, *Lab Chip*, 2021, **21**, 3053–3075.
13 V. A. Bot, A. Shakeri, J. I. Weitz and T. F. Didar, *Adv. Funct. Mater.*, 2022, **32**, 2205078.
14 T. F. Didar and M. Tabrizian, *Lab Chip*, 2012, **12**, 4363–4371.
15 A. Shakeri, N. Sun, M. Badv and T. F. Didar, *Biomicrofluidics*, 2017, **11**, 044111.
16 T. F. Didar, K. Bowey, G. Almazan and M. Tabrizian, *Adv. Healthcare Mater.*, 2014, **3**, 253–260.
17 T. F. Didar and M. Tabrizian, *Lab Chip*, 2010, **10**, 3043–3053.
18 T. F. Didar, K. Li, T. Veres and M. Tabrizian, *Biomaterials*, 2013, **34**, 5588–5593.
19 T. F. Didar, K. Li, M. Tabrizian and T. Veres, *Lab Chip*, 2013, **13**, 2615–2622.
20 S. Antona, T. Abele, K. Jahnke, Y. Dreher, K. Göpfrich, I. Platzman and J. P. Spatz, *Adv. Funct. Mater.*, 2020, **30**, 2003479.
21 S. Antona, I. Platzman and J. P. Spatz, *ACS Omega*, 2020, **5**, 24674–24683.
22 N. Subedi, L. C. Van Eyndhoven, A. M. Hokke, L. Houben, M. C. Van Turnhout, C. V. C. Bouten, K. Eyer and J. Tel, *Sci. Rep.*, 2021, **11**, 17084.
23 N. Subedi, L. P. Verhagen, P. de Jonge, L. C. Van Eyndhoven, M. C. van Turnhout, V. Koomen, J. Baudry, K. Eyer, H. Dolstra and J. Tel, *Adv. Biol.*, 2023, **7**, 2200207.
24 D. Ravi, S. Sarkar, S. Purvey, F. Passero, A. Beheshti, Y. Chen, M. Mokhtar, K. David, T. Konry and A. M. Evens, *Leukemia*, 2020, **34**, 1291–1304.
25 M. R. Sullivan, M. Finocchiaro, Y. Yang, J. Thomas, A. Ali, I. Kaplan, Y. Abdulhamid, E. Bobilev, M. Sheffer, R. Romee and T. Konry, *J. Immunother. Cancer*, 2024, **12**, e008912.
26 S. N. Agnihotri, G. S. Ugolini, M. R. Sullivan, Y. Yang, A. De Ganzó, J. W. Lim and T. Konry, *Lab Chip*, 2022, **22**, 3258–3267.
27 S. Sarkar, W. Kang, S. Jiang, K. Li, S. Ray, E. Luther, A. R. Ivanov, Y. Fu and T. Konry, *Lab Chip*, 2020, **20**, 2317–2327.
28 M. R. Sullivan, R. P. White, D. Ravi, N. Kanetkar, I. B. Fridman, A. Ekenseair, A. M. Evens and T. Konry, *Cell Death Dis.*, 2024, **15**, 1–9.
29 F. Aubermann, S. Seneca, T. Hofman, I. Garcés-Lázaro, K. Ajmail, K. Daubner, A. Cerwenka, I. Platzman and J. P. Spatz, *Small Methods*, 2025, **9**, 2500236.
30 K. Gardner, M. M. Uddin, L. Tran, T. Pham, S. Vanapalli and W. Li, *Lab Chip*, 2022, **22**, 4067–4080.
31 H. Sun, W. Xie, J. Mo, Y. Huang and H. Dong, *Front. Bioeng. Biotechnol.*, 2023, **11**, 1208648.
32 E. Liu, D. Marin, P. Banerjee, H. A. Macapinlac, P. Thompson, R. Basar, L. N. Kerbauy, B. Overman, P. Thall, M. Kaplan, V. Nandivada, I. Kaur, A. N. Cortes, K. Cao, M. Daher, C. Hosing, E. N. Cohen, P. Kebriaei, R. Mehta, S. Neelapu, Y. Nieto, M. Wang, W. Wierda, M. Keating, R. Champlin, E. J. Shpall and K. Rezvani, *N. Engl. J. Med.*, 2020, **382**, 545–553.
33 M. M. Berrien-Elliott, M. T. Jacobs and T. A. Fehniger, *Blood*, 2023, **141**, 856–868.
34 J. S. Orange, *Nat. Rev. Immunol.*, 2008, **8**, 713–725.
35 R. J. A. Maas, J. S. Hoogstad-van Evert, I. M. Hagemans, J. Brummelman, D. van Ens, P. K. J. D. de Jonge, L. Hooijmaijers, S. Mahajan, A. B. van der Waart, C. K. J. C. Hermans, J. de Klein, R. Woestenenk, A. E. van Herwaarden, N. P. M. Schaap, S. Rezaeifard, D. V. F. Tauriello, P. L. M. Zusterzeel, N. Ottevanger, J. H. Jansen, W. Hobo and H. Dolstra, *Front. Immunol.*, 2024, **15**, 1448041.
36 C. R. Tonetti, C. N. de Souza-Araújo, A. Yoshida, R. F. da Silva, P. C. M. Alves, T. N. Mazzola, S. Derchain, L. G. R. Fernandes and F. Guimarães, *Cell*, 2021, **10**, 1702.
37 N. Bougen-Zhukov, S. Y. Loh, H. K. Lee and L.-H. Loo, *Cytometry, Part A*, 2017, **91**, 115–125.
38 D. M. Davis, I. Chiu, M. Fassett, G. B. Cohen, O. Mandelboim and J. L. Strominger, *Proc. Natl. Acad. Sci. U. S. A.*, 1999, **96**, 15062–15067.
39 A. Schietinger, M. Philip, R. B. Liu, K. Schreiber and H. Schreiber, *J. Exp. Med.*, 2010, **207**, 2469–2477.
40 A. Stojanovic and A. Cerwenka, *J. Innate Immun.*, 2011, **3**, 355–364.
41 R. Bhat and C. Watzl, *PLoS One*, 2007, **2**, e326.
42 M. M. Gubin, X. Zhang, H. Schuster, E. Caron, J. P. Ward, T. Noguchi, Y. Ivanova, J. Hundal, C. D. Arthur, W.-J. Krebber, G. E. Mulder, M. Toebes, M. D. Vesely, S. S. K. Lam, A. J. Korman, J. P. Allison, G. J. Freeman, A. H. Sharpe, E. L. Pearce, T. N. Schumacher, R. Aebersold, H.-G. Rammensee, C. J. M. Melief, E. R. Mardis, W. E. Gillanders, M. N. Artyomov and R. D. Schreiber, *Nature*, 2014, **515**, 577–581.
43 K. Guldevall, L. Brandt, E. Forslund, K. Olofsson, T. W. Frisk, P. E. Olofsson, K. Gustafsson, O. Manneberg, B. Vanherberghen, H. Brismar, K. Kärre, M. Uhlin and B. Önfelt, *J. Innate Immun.*, 2016, **7**, 119.
44 G. Romain, V. Senyukov, N. Rey-Villamizar, A. Merouane, W. Kelton, I. Liadi, A. Mahendra, W. Charab, G. Georgiou, B. Roysam, D. A. Lee and N. Varadarajan, *Blood*, 2014, **124**, 3241–3249.

 This journal is © The Royal Society of Chemistry 2026

45 J. Xiao, T. Zhang, F. Gao, Z. Zhou, G. Shu, Y. Zou and G. Yin, *Cancers*, 2022, **14**, 5657.
46 R. J. Beck, D. I. Bijker and J. B. Beltman, *PLoS Comput. Biol.*, 2020, **16**, e1007972.
47 S. Paul and G. Lal, *J. Innate Immun.*, 2017, **8**, 1124.
48 H. Li, Y. Han, Q. Guo, M. Zhang and X. Cao, *J. Immunol.*, 2009, **182**, 240–249.
49 H. Klingemann, L. Boissel and F. Toneguzzo, *J. Innate Immun.*, 2016, **7**, 91.
50 P. Parham, *Nat. Rev. Immunol.*, 2005, **5**, 201–214.

Open Access Article. Published on 13 May 2026. Downloaded on 6/3/2026 1:05:32 PM.
This article is licensed under a Creative Commons Attribution 3.0 Unported Licence.